Tidal Mixing in the South China Sea: An Estimate Based on the Internal Tide Energetics

XIAOWEI WANG

State Key Laboratory of Tropical Oceanography, South China Sea Institute of Oceanology, Chinese Academy of Sciences, Guangzhou, and University of Chinese Academy of Sciences, Beijing, China

SHIQIU PENG

State Key Laboratory of Tropical Oceanography, South China Sea Institute of Oceanology, Chinese Academy of Sciences, Guangzhou, and Laboratory for Regional Oceanography and Numerical Modeling, Qingdao National Laboratory for Marine Science and Technology, Qingdao, China

ZHIYU LIU

State Key Laboratory of Marine Environmental Science, and Department of Physical Oceanography, College of Ocean and Earth Sciences, Xiamen University, Xiamen, China

RUI XIN HUANG

Department of Physical Oceanography, Woods Hole Oceanographic Institution, Woods Hole, Massachusetts

YU-KUN QIAN AND YINENG LI

State Key Laboratory of Tropical Oceanography, South China Sea Institute of Oceanology, Chinese Academy of Sciences, Guangzhou, China

(Manuscript received 28 April 2015, in final form 13 October 2015)

ABSTRACT

By taking into account the contributions of both locally and remotely generated internal tides, the tidal mixing in the Luzon Strait (LS) and the South China Sea (SCS) is investigated through internal-tide simulation and energetics analysis. A three-dimensional nonhydrostatic high-resolution model driven by four primary tidal constituents (M_2, S_2, K_1, and O_1) is used for the internal-tide simulation. The baroclinic energy budget analysis reveals that the internal tides radiated from the LS are the dominant energy source for the tidal dissipation in the SCS. In the LS, the estimated depth-integrated turbulent kinetic energy dissipation exceeds $O(1)$ W m^{-2} atop the two subsurface ridges, with a dissipation rate of $>O(10^{-7})$ W kg^{-1} and diapycnal diffusivity of $\sim O(10^{-2})$ m^2 s^{-1}. In the SCS, the most intense turbulence occurs in the deep-water basin with a dissipation rate of $O(10^{-8}$–$10^{-6})$ W kg^{-1} and diapycnal diffusivity of $O(10^{-3}$–$10^{-1})$ m^2 s^{-1} within the $\sim$2000-m water column above the seafloor as well as in the shelfbreak region with a dissipation rate of $O(10^{-7}$–$10^{-6})$ W kg^{-1} and diapycnal diffusivity of $O(10^{-4}$–$10^{-3})$ m^2 s^{-1}. These estimated values are consistent with observations reported in previous studies and are at least one order of magnitude larger than those based solely on locally generated internal tides.

1. Introduction

Turbulent mixing is of vital importance in many aspects of ocean dynamics. The return pathways of deep water to their formation regions, involved in the global meridional overturning circulation (MOC), include both the adiabatic wind-driven upwelling in the Southern Ocean and the diabatic diapycnal mixing in the deep Indian and Pacific Oceans (Marshall and Speer 2012; Talley 2013). Thus, diapycnal mixing plays a key role in maintaining the ocean stratification and MOC and could in turn significantly impact both local and global climate through heat transport (Rahmstorf 2003). It was estimated that the globally averaged diapycnal diffusivity

necessary to maintain the observed abyssal stratification is of $O(10^{-4})\,m^2\,s^{-1}$ (Munk and Wunsch 1998). However, the spatial distribution of diapycnal diffusivity is highly inhomogeneous; while smaller values of $\sim O(10^{-5})\,m^2\,s^{-1}$ are found in the ocean interior far from boundaries (e.g., Ledwell et al. 1993; Polzin et al. 1997), larger values of $\sim O(10^{-2}\text{–}10^{-3})\,m^2\,s^{-1}$ have been observed over seamounts, ridges, canyons, and hydraulically controlled passages in open oceans (e.g., Kunze and Toole 1997; Ledwell et al. 2000; Carter and Gregg 2002; Ferron et al. 1998) as well as continental shelves in marginal seas (e.g., MacKinnon and Gregg 2003), where enhanced diapycnal mixing occurs.

Enhanced diapycnal mixing is largely sustained by breaking internal waves in the ocean interior, including near-inertial waves generated by wind stress on the surface, baroclinic tides (internal waves with tidal frequencies, also called internal tides) induced by the interaction of barotropic tides with rough topography, and internal lee waves generated by quasi-steady flow over rough topography in the stratified ocean (MacKinnon 2013). Wunsch and Ferrari (2004) postulated that the wind energy input is dissipated mostly within the upper ocean, with only a very small portion entering the layers below; there is, however, an ongoing debate with regard to how deep the wind energy input can penetrate. The global energy input into internal lee waves is estimated at the range of 0.2–0.4 TW, and the strongest generation area is the Southern Ocean, where the strong Antarctic Circumpolar Current flows over rough topography (Nikurashin and Ferrari 2013; Scott et al. 2011). The energy conversion from barotropic tides to internal tides in the deep ocean has been estimated as 1 TW (Egbert and Ray 2000), which is about a third of the total dissipation of barotropic tides in the global ocean, providing half of the 2 TW necessary to maintain the MOC (Munk and Wunsch 1998). Therefore, internal tides are the primary source of mechanical energy for diapycnal mixing in the deep ocean.

The South China Sea (SCS) is the largest marginal sea in the western Pacific. The Luzon Strait (LS) is the only deep-water passage between the Pacific and the SCS. Elevated diapycnal mixing in the LS and SCS, up to $10^{-3}\,m^2\,s^{-1}$, has been reported in recent studies (St. Laurent 2008; St. Laurent et al. 2011; Lozovatsky et al. 2013; Yang et al. 2014). Observations show an overflow from the Pacific into the SCS in the deep layer and an outflow from the SCS to the Pacific via the midlayer of LS (Tian et al. 2006; Chang et al. 2010; Zhao et al. 2014). Inside the SCS deep water is lightened through diapycnal mixing with the warmer and fresher water overlying, driving an upwelling within the deep basin (Qu et al. 2006). It is thus clear that enhanced diapycnal mixing in the LS and SCS plays a key role in driving the SCS circulation and maintaining the abyssal water transport through the LS.

Intensive diapycnal mixing in the LS and SCS is mostly due to baroclinic tidal dissipation in this domain (Alford et al. 2011, 2015; Klymak et al. 2011). Energetic internal tides in this region have been captured by in situ observations (e.g., Guo et al. 2012; Ma et al. 2013) and remotely sensed images (Zhao 2014). The LS is featured with two submarine ridges, which consist of several islands. Strong internal tides are generated as tidal currents flow over these complicated and rough topographies. Subsequently, part of the internal tides is dissipated locally near the generation sites and the remaining part propagates eastward into the northwest Pacific and westward into the SCS, fertilizing the diapycnal mixing there (Niwa and Hibiya 2004; Chao et al. 2007; Jan et al. 2007, 2008). With the steep continental slope and numerous seamounts, the extremely complicated topographies make the SCS a preferred region for dissipation of internal tides generated both locally and remotely. However, because of the lack of sufficient in situ data for internal tides generated in the LS and SCS, especially in the deep water, some important issues still remain open, such as what the fraction of energy dissipated locally in the LS is, how far the internal tides can propagate across the SCS, what their vertical decay structures are, and where they eventually dissipate in the vast basin of the SCS. Therefore, to understand and parameterize the diapycnal mixing in the LS and SCS, a better understanding of the energetics of internal tides in this region is required.

The vertical resolution of most state-of-the-art ocean climate models is too coarse to directly simulate diapycnal mixing induced by internal wave breaking. Parameterization of diapycnal diffusivities is thus needed in these models to represent the mixing process more accurately. Previous studies indicated that parameterization of diapycnal diffusivities is crucial for realistic simulation of circulation, heat transport, water mass transformation, and storage of carbon dioxide (e.g., Friedrich et al. 2011). Given that ocean mixing is maintained by external mechanical energy (Huang 1999; Wunsch and Ferrari 2004; MacKinnon 2013), the energetics constraint is thus essential in developing a turbulence parameterization in large-scale ocean models.

In the early stage of model development, a constant or a horizontally uniform vertical profile of diapycnal diffusivity was set in ocean models (e.g., Bryan and Lewis 1979). The most popular vertical mixing parameterization schemes currently used in ocean numerical simulations are the Pacanowski and Philander (1981) (PP), Mellor and Yamada (1982) (MY), and K-profile parameterization (KPP) (Large et al. 1994) schemes. In

applying a turbulent mixing scheme for the ocean, a vitally important point is to make sure that all the external mechanical energy required for sustaining the turbulence must be included. However, none of the turbulence schemes listed above were developed in terms of the external mechanical energy input, and thus they may not represent the turbulent mixing correctly.

An estimate of tidal mixing should include energy conversion from barotropic to baroclinic tides, as well as the breaking and dissipation processes of internal tides; however, our understanding of these processes remains rudimentary. St. Laurent et al. (2002, hereinafter LSJ02) proposed a semiempirical scheme for parameterization of the diapycnal mixing driven by the dissipation of internal tides near their generation sites. Accordingly, the internal-tide generation is calculated using the linear theory of Bell (1975) and is based on an approximation suitable for subcritical topography (Jayne and St. Laurent 2001). The dissipation process is parameterized by a uniformly set fraction of energy locally dissipated and an exponential vertical decay structure with a specified vertical scale, which was chosen to be consistent with observations (Polzin et al. 1997; Ledwell et al. 2000). Recently, Polzin (2009) formulated a refined prediction for the internal wave dissipation, which was linked to the finescale internal wave shear based on a theory of weak nonlinear interactions between the generated waves and the ambient wave field (Polzin 2004). The LSJ02 parameterization has been implemented in several ocean general circulation models to investigate the impact of tidal mixing on the stratification, circulation, and heat transport of global open oceans (e.g., Simmons et al. 2004; Saenko and Merryfield 2005; Jayne 2009; Melet et al. 2013).

The LSJ02 scheme, however, considers solely the dissipation of locally generated internal tides, whereas the dissipation of remotely generated internal tides is ignored. For such marginal seas as the SCS, most of internal tides are not locally generated; instead, they are generated from the adjacent prominent bathymetry (e.g., the LS). Therefore, the energy input from the dissipation of both locally and remotely generated internal tides (hereinafter called local tidal dissipation and remote tidal dissipation, respectively) should be taken into account in the estimate of turbulent mixing in the region. Currently, however, because of the lack of a deep understanding of the physical and dynamic features of these phenomena, it is difficult to parameterize the turbulent mixing induced by both local and remote tidal dissipation with a universal formula. Instead, an analysis of energetics of internal tides with numerical simulations is a natural step toward developing an energy-constrained turbulence parameterization, which is the subject of this investigation.

The purpose of this paper is to investigate the tidal dissipation and mixing processes in the LS and SCS, taking into account the effect of both locally and remotely generated internal tides. First, we use a three-dimensional nonhydrostatic baroclinic tide model with high spatial–temporal resolution to simulate the generation and propagation processes of internal tides across the entire SCS and LS region with four primary tidal constituents (M_2, S_2, K_1, and O_1). Then we analyze the baroclinic energy budget using the depth-integrated baroclinic energy equation and compare our results with those calculated by the LSJ02 parameterization to discuss the effect of remotely generated internal tides on the dissipation in the SCS. Finally, we provide the preliminary three-dimensional climatological fields of dissipation rate and diapycnal diffusivity for the entire SCS and LS region.

This study is organized as follows: The baroclinic tide model configuration is described in section 2. The LSJ02 parameterization and the baroclinic energy budget analysis method are given in section 3. The energy budget of internal tides and the distributions of dissipation rate and diapycnal diffusivity are presented in section 4. Finally, section 5 is the summary and discussion.

2. Baroclinic tide model configuration

The ocean model used in this study is the Massachusetts Institute of Technology General Circulation Model (MITgcm) (Marshall et al. 1997). This model has been widely used for researches on internal-tide generation, propagation, and dissipation over rough topography (e.g., Buijsman et al. 2012, 2014). Our model domain is from 1.5° to 29.5°N and from 98.5° to 128.5°E, covering the SCS, LS, and part of the northwest Pacific. The model topography is taken from the General Bathymetric Chart of the Oceans (GEBCO_08) bathymetry data (http://www.gebco.net/) with a high resolution of 30 arc s (Fig. 1a). The horizontal resolution of our model is $\frac{1}{24}° \times \frac{1}{24}°$ over the entire domain. There are 60 z levels in the vertical direction; the thicknesses of the top 12 levels are 10 m near the surface and gradually increase to 50 m in the upper 300 m, followed by 42 levels with 100-m resolution and finally the bottom 6 levels with 200-m resolution (Fig. 1b).

The initial temperature and salinity profiles are derived from the monthly mean climatology of Generalized Digital Environmental Model, version 3 (GDEMv3) (http://www.usgodae.org/pub/outgoing/static/ocn/gdem/), near the site 20.5°N, 120.25°E; thus, the initial density of the baroclinic tide model is horizontally homogeneous and vertically stratified. The profiles within the upper
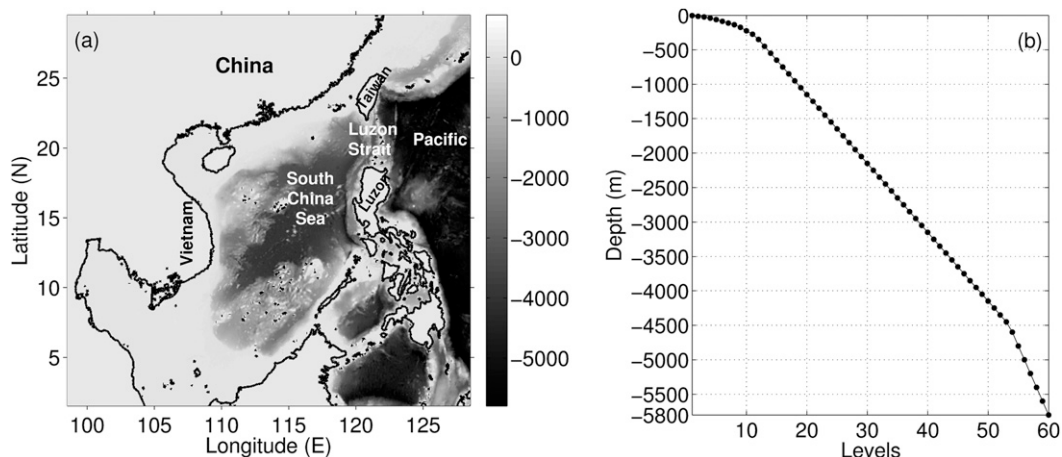
FIG. 1. (a) Bathymetry of the model domain and (b) depth of the model levels.

500 m are quite different for the winter (January) and summer (July) seasons (Fig. 2). The pycnocline is broader and stronger in summer with the maximum value of the squared buoyancy frequency up to $3 \times 10^{-4} \, \text{s}^{-2}$. Large phase offset of internal tides in the SCS between winter and summer has been observed by satellite altimetry (Ray and Zaron 2011). Thus, two simulations are carried out for these two seasons with different stratifications, so as to investigate the seasonal variations in internal-tide generation, propagation, and dissipation, and the mean of these two seasons is taken as the annual-mean climatology.

The model is forced by four primary tidal constituents (M_2, S_2, K_1, and O_1) at the open boundaries. The amplitudes and phases are extracted from the regional solution for the China Sea of the Oregon State University (OSU) inverse barotropic tidal model (OTIS) (Egbert et al. 1994; Egbert and Erofeeva 2002) with $\frac{1}{30}°$ spatial resolution (http://volkov.oce.orst.edu/tides/YS.html). Furthermore, at each of the open boundaries, a 0.5° width sponge layer is imposed to avoid artificial reflection. To simplify the related analysis, no turbulence closure is adopted in the simulations. The diffusion of temperature and salinity is ignored by setting the horizontal and vertical diffusivities as $K_h = K_v = 0$. A horizontal viscosity of $A_h = 10 \, \text{m}^2 \, \text{s}^{-1}$, a vertical viscosity of $A_v = 1 \times 10^{-4} \, \text{m}^2 \, \text{s}^{-1}$, and a bottom drag coefficient of $C_d = 2.5 \times 10^{-3}$ are specified uniformly throughout the domain. Through a set of sensitivity experiments, we found that the baroclinic energy
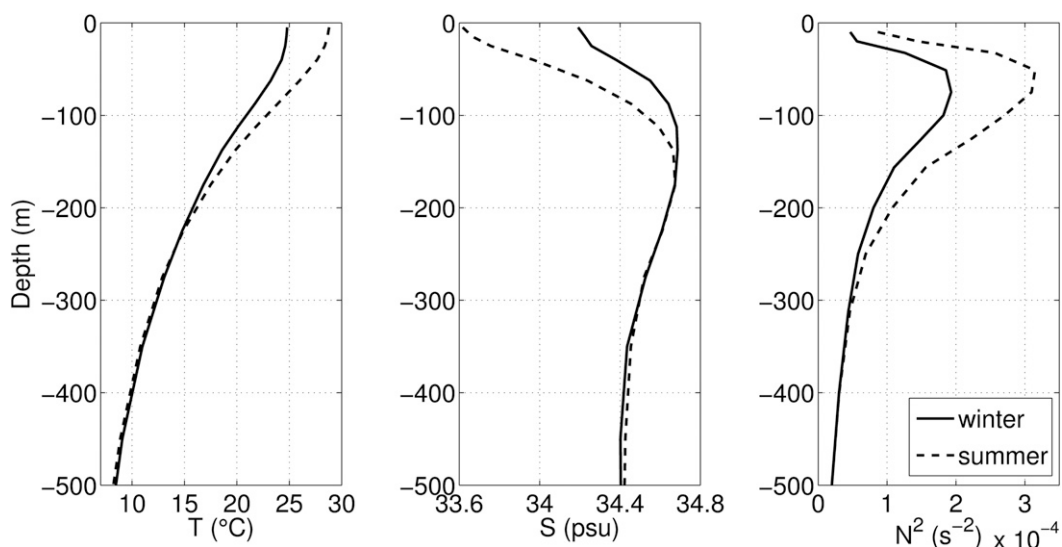
FIG. 2. Temperature T, salinity S, and corresponding squared buoyancy frequency N^2 profiles used as the initial fields in winter (solid lines) and summer (dashed lines) runs.

budget is not significantly affected by the employed values of viscosity and bottom drag coefficient (see the appendix).

Simulations for the two seasons both start from a state of rest, using a time step of 90 s. It takes about 10 days for the internal tides originated in the LS to reach a steady state near the farthest boundary. Therefore, the integrated time is set to 30 days to cover a spring–neap tidal cycle for each season; two 2-day time series of hourly model results during a spring tide and a neap tide, respectively, are used for energy budget analysis, and their averages are taken as the seasonal means.

3. Estimate methods

a. LSJ02 parameterization

The LSJ02 parameterization scheme for estimating the diapycnal mixing induced by internal tides is formulated as

$$\kappa_v \simeq \frac{\Gamma q E(x, y) F(z)}{\rho N^2} + \kappa_0. \tag{1}$$

Here, $E(x, y)$ is the energy flux per unit area transferred from barotropic to baroclinic tides, and the fraction of which are likely to dissipate near-internal-tide generation sites is given by the local dissipation efficiency q [here chosen as $q = 0.3$, as suggested by LSJ02]. The term $F(z)$ is a structure function representing the vertical distribution of the turbulent dissipation rate. The quantity Γ is the mixing efficiency (Osborn 1980), κ_0 is the background diffusivity, ρ is the density of seawater, and N^2 is the squared buoyancy frequency.

The internal-tide energy flux $E(x, y)$ is given by Jayne and St. Laurent (2001):

$$E(x, y) \simeq \frac{1}{2} \rho_0 N_b k h^2 \langle u_{bt}^2 \rangle, \tag{2}$$

where ρ_0 is the reference density of seawater, and N_b is the buoyancy frequency at the seafloor, both of which are calculated from GDEMv3 database in this study. The terms k and h are the wavenumber and amplitude scales for the topographic roughness. Here, h^2 is computed as the mean-square of height deviations from a polynomial sloping surface fit ($H = a + bx + cy + dxy$) of the topography to a plane over a grid box using the GEBCO_08 bathymetric dataset, and k is a spatial constant, set as $k = 2\pi/(5\,\text{km})$ throughout the domain. The term $\langle u_{bt}^2 \rangle$ is the tidal period mean of squared barotropic tidal speed computed from our model results.

Based on turbulent observations from the abyssal ocean and continental slope, LSJ02 suggested the dissipation rate

be modeled as a simple exponential function that decays upward away from the bottom topography, and this gives the vertical structure function

$$F(z) = \frac{\exp[-(D + z)/\zeta]}{\zeta[1 - \exp(-D/\zeta)]} \tag{3}$$

to satisfy the energy conservation within an integrated vertical column, where D is the total depth of the water column, and ζ is the vertical decay scale.

b. Baroclinic energy budget analysis method

Following Niwa and Hibiya (2004), the internal tides energy can be analyzed quantitatively, using the depth-integrated baroclinic energy equation

$$\text{TEN}_{bc} = -\nabla_h \cdot \mathbf{F}_{bc} + E_{bt2bc} + \text{ADV}_{bc} + \text{DIS}_{bc}, \tag{4}$$

where $\mathbf{F}_{bc}$ is the depth-integrated baroclinic energy flux, and TEN_{bc}, ADV_{bc}, and DIS_{bc} denote the tendency, the advection, and the dissipation of baroclinic energy, respectively. Assuming that the tidal period mean of baroclinic energy density is unchanged within a fixed area and the advection of baroclinic energy is negligible, the tidal period mean of the depth-integrated dissipation rate of baroclinic energy can be approximated as

$$\langle \text{DIS}_{bc} \rangle \approx -\langle E_{bt2bc} \rangle + \langle \nabla_h \cdot \mathbf{F}_{bc} \rangle, \tag{5}$$

where $\langle \cdot \rangle$ represents the tidal period mean. The depth-integrated conversion from barotropic to baroclinic energy E_{bt2bc} and the divergence of the depth-integrated baroclinic energy flux $\nabla_h \cdot \mathbf{F}_{bc}$ are given by

$$E_{bt2bc} = g \int_{-H}^{\eta} \rho' w_{bt}\, dz, \quad \text{and} \tag{6}$$

$$\nabla_h \cdot \mathbf{F}_{bc} = \nabla_h \cdot \left(\int_{-H}^{\eta} \mathbf{u}' p'\, dz \right), \tag{7}$$

where H and η denote the time-mean water depth and the sea level displacement, respectively; w_{bt} is the vertical velocity induced by the barotropic flow; and ρ', p', and $\mathbf{u}' = (u', v')$ are the density perturbation, pressure perturbation, and horizontal baroclinic velocity, respectively. It should be noted that the baroclinic energy dissipation $\langle \text{DIS}_{bc} \rangle$ obtained by Eq. (5) may include both the physical dissipation and the biases due to the numerical dissipation and computation errors (e.g., the neglected terms of the energy budget) and thus could be somewhat overestimated. However, given that $\langle \text{DIS}_{bc} \rangle$ obtained by Eq. (5) is virtually independent of the dissipation parameters (A_h, A_v, and C_d) (see the appendix for details), Eq. (5)

is still a good approximation for estimating the baroclinic energy dissipation.

The vertical velocity w_{bt} can be computed as follows (Mellor 2004):

$$w_{bt} = U\left(\sigma\frac{\partial D}{\partial x} + \frac{\partial \eta}{\partial x}\right) + V\left(\sigma\frac{\partial D}{\partial y} + \frac{\partial \eta}{\partial y}\right) + (\sigma + 1)\frac{\partial \eta}{\partial t}, \tag{8}$$

where U and V are the barotropic velocities in the x and y directions, respectively; D is the total water depth $D = H + \eta$; and σ is defined as $\sigma = (z - \eta)/D$.

The density perturbation ρ', pressure perturbation p', and horizontal baroclinic velocity $\mathbf{u}'$ are computed following the work of Nash et al. (2005). First, the density perturbation is defined as

$$\rho'(z,t) = \rho(z,t) - \langle\rho\rangle(z), \tag{9}$$

where ρ is the instantaneous density, and $\langle\rho\rangle$ is the tidal period mean of the vertical density profile. Using the hydrostatic equation, the pressure perturbation is expressed as

$$p'(z,t) = p'_{surf}(t) + \int_z^\eta \rho'(\hat{z},t)g\,d\hat{z}, \tag{10}$$

where the surface pressure $p'_{surf}(t)$ is inferred from the baroclinicity condition that the depth-averaged pressure perturbation must vanish:

$$\frac{1}{H}\int_{-H}^\eta p'(z,t)\,dz = 0. \tag{11}$$

Thus, the pressure perturbation can be calculated as

$$p'(z,t) = -\frac{1}{H}\int_{-H}^\eta\int_z^\eta g\rho'(\hat{z},t)\,d\hat{z}\,dz + \int_z^\eta g\rho'(\hat{z},t)\,d\hat{z}. \tag{12}$$

The baroclinic velocity is defined as

$$\mathbf{u}'(z,t) = \mathbf{u}(z,t) - \langle\mathbf{u}\rangle(z) - \mathbf{u}_{bt}(t), \tag{13}$$

where $\mathbf{u}$ is the instantaneous velocity vector, $\langle\mathbf{u}\rangle$ is the tidal period mean of the velocity, and the barotropic velocity $\mathbf{u}_{bt} = (U, V)$ is determined by the baroclinicity condition that the depth-averaged baroclinic velocity must vanish:

$$\frac{1}{H}\int_{-H}^\eta \mathbf{u}'(z,t)\,dz = 0. \tag{14}$$

Thus, the barotropic and baroclinic velocity can be calculated as

$$\mathbf{u}_{bt}(t) = \frac{1}{H}\int_{-H}^\eta [\mathbf{u}(z,t) - \langle\mathbf{u}\rangle(z)]\,dz, \quad \text{and} \tag{15}$$

$$\mathbf{u}'(z,t) = \mathbf{u}(z,t) - \langle\mathbf{u}\rangle(z) - \frac{1}{H}\int_{-H}^\eta [\mathbf{u}(z,t) - \langle\mathbf{u}\rangle(z)]\,dz. \tag{16}$$

Currently, because of the lack of substantial microstructure observations, the vertical distribution of energy dissipation due to the remotely generated internal tide remains elusive. Thus, we adopt the vertical structure function $F(z)$ in LSJ02 parameterization, given as Eq. (3), and assume both the local and remote tidal dissipation to be a bottom-intensified exponential profile with an e-folding scale $\zeta = 500$ m as in LSJ02. Following the formulation by Osborn (1980), the diapycnal diffusivity driven by the dissipation of locally and remotely generated internal tide can thus be calculated by

$$\kappa_v = \frac{\Gamma\langle DIS_{bc}\rangle F(z)}{\rho N^2} + \kappa_0, \tag{17}$$

where the mixing efficiency Γ is taken to be the canonical value of $\Gamma = 0.2$ (Osborn 1980), and the background diffusivity is assumed to be a constant $\kappa_0 = 1 \times 10^{-5}$ m^2 s^{-1}. The density of seawater ρ and the squared buoyancy frequency N^2 are calculated from the annual-mean climatology of GDEMv3 data.

4. Results

a. Basic properties

It is important to check if the model simulates the barotropic tide reasonably well before analyzing the baroclinic tide properties. A barotropic tide model for the diagnosis is run, forced by each of the four primary tidal constituents at the open boundaries. Figure 3 shows the barotropic tidal energy fluxes that are calculated by $\mathbf{P} = \rho g h\langle\mathbf{u}_{bt}\eta\rangle$ for the four primary tidal constituents. The westward vectors of energy fluxes around the LS suggest that the barotropic tidal energy enters the SCS from the Pacific through the LS. Inside the SCS, the propagation directions of all tidal waves shift southwestward. The meridional section-integrated energy fluxes across the LS for the constituents M_2, S_2, K_1, and O_1 reach 35.11, 3.59, 24.42, and 16.98 GW, respectively. The distribution patterns of barotropic tidal energy fluxes from our model results are similar to those of the OTIS data (not shown) throughout the SCS and LS region and the relative rms errors of flux magnitude for M_2, S_2, K_1, and O_1 are 6%, 7%, 11%, and 2%, respectively.

The spatial–temporal distributions of internal tidal signals generated by the combined four primary tidal
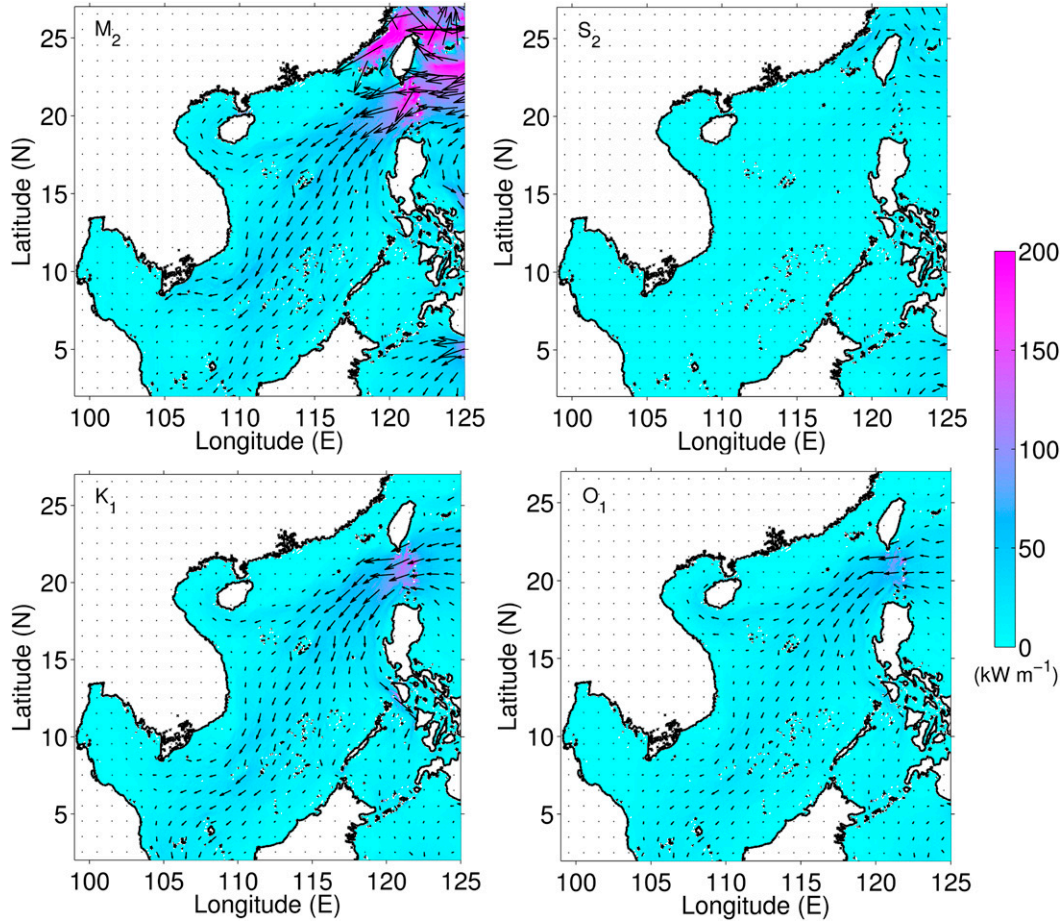
FIG. 3. Barotropic tidal energy flux (vector) and its magnitude (color shading) for the four primary constituents M_2, S_2, K_1, and O_1.

constituents are shown in Fig. 4. The near-surface pressure perturbations, with an amplitude of 800 Pa near the LS, clearly show that the internal tides generated in the LS propagate eastward and westward, suggesting that the LS is the main source region of internal tides for the SCS and one of the most important source areas for the northwest Pacific (Niwa and Hibiya 2014). The westward internal tides travel across the central deep basin of the SCS and arrive at the surrounding continental slope, mainly confined in regions deeper than the 200-m isobath. It is generally consistent with the pattern described by Zhao (2014), using the surface height observations collected by multiple satellites. The vertical structure of baroclinic velocity exhibits that the strongest internal tidal currents occur in the near-surface layer, with velocities exceeding $1\,\mathrm{m\,s^{-1}}$, and there is also pronounced near-bottom intensification, showing a good agreement with previous mooring observations (Duda and Rainville 2008; Klymak et al. 2011). The diurnal (semidiurnal) signals in the spring (neap) tides exhibit in the temporal variations of

baroclinic velocity, suggesting that diurnal tidal currents are stronger (weaker) than the semidiurnal currents during spring (neap) tides. Moreover, baroclinic tides are stronger in summer because of the stronger stratification.

b. Baroclinic energy budget

Figure 5 illustrates the energy budget of internal tides in the SCS and LS based on the combined four primary tidal constituents, including the area-integrated conversion from barotropic to baroclinic tidal energy (Conv), divergence of baroclinic energy flux (DivF) and dissipation rate of the baroclinic energy (Diss), as well as the meridional section-integrated baroclinic energy on the western, (F_{west}), and eastern, (F_{east}), boundaries of the area. Generally speaking, the value of each term of the energy budget in summer is greater than that in winter; in addition, in each season the value of each term during the spring tide is larger than that during the neap tide. Stronger stratification in the summertime thermocline is favorable for the energy cascade from barotropic to baroclinic tides and the growth of baroclinic
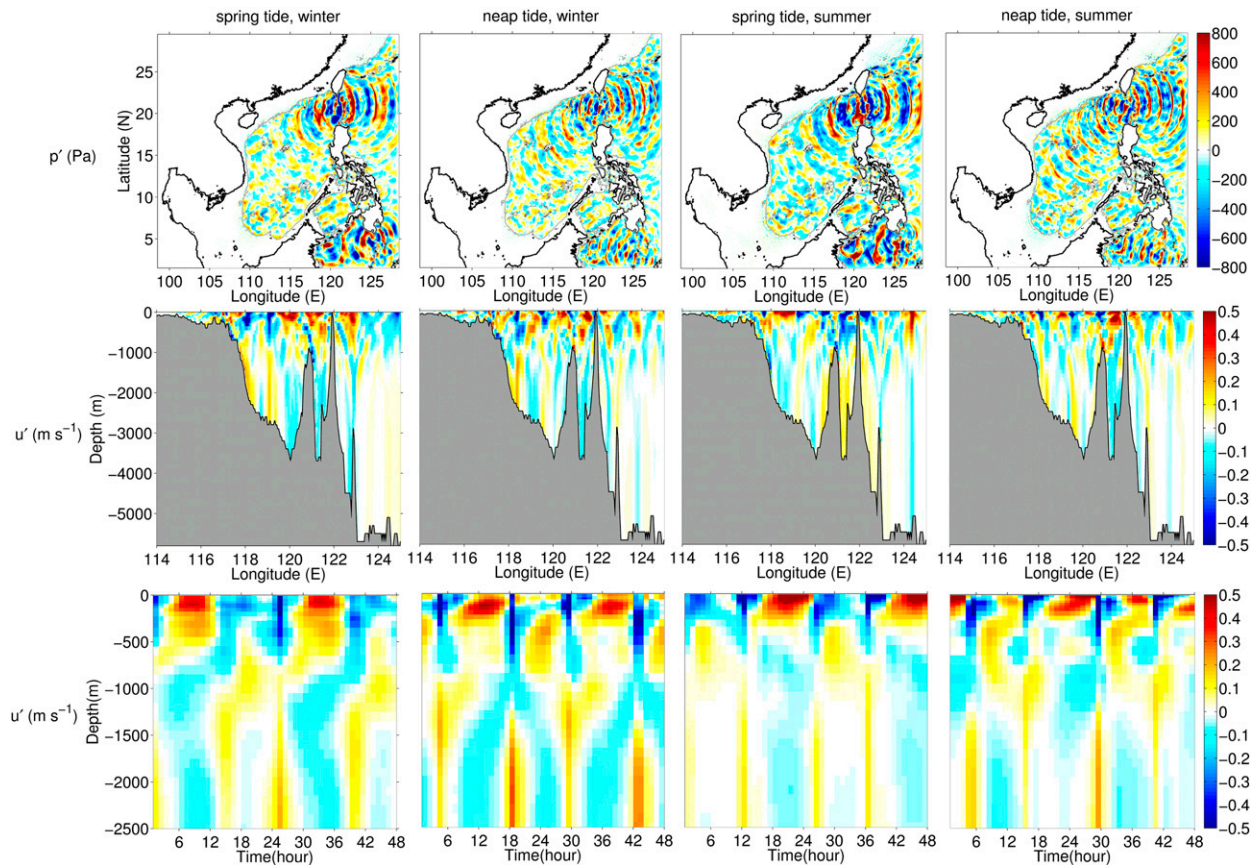
FIG. 4. (top) Instantaneous near-surface pressure perturbation p', (middle) zonal baroclinic velocity u' along 21°N, and (bottom) the time variation of u' at site 21°N, 119°E during the spring–neap tides in winter/summer. The gray contours in the top row represent the 200-m isobath.

instability, leading to higher efficiency of the energy transformation and enhanced energy dissipation in summer.

In the LS, over the spring–neap cycle for both summer and winter, the Conv is about 24.9–41.1 GW, 37%–40% ($\sim$9.7–15.3 GW) of which is locally dissipated (Diss) and about 8.5–13.0 GW propagates westward into the SCS (F_{west}). In comparison with the winter season, during the summer season about 8% more barotropic tidal energy is converted to baroclinic energy, 7% more baroclinic energy is dissipated locally, and 10% more energy is propagated into the SCS. The magnitude of the energy budget in our estimation is close to several previous modeling studies for this region. Using a similar linear damping scheme, Niwa and Hibiya (2004) predicted 37% local dissipation for M_2. Jan et al. (2008) presented conversion values ranging from 11.0 to 50.4 GW for the four combined primary tidal constituents with 57%–60% local dissipation and 2.5–10.8-GW energy propagating westward into the SCS. Alford et al. (2011) reported the total modeled conversion of 24.1 GW for semidiurnal and

diurnal bands, with 39% local dissipation. Kerry et al. (2013) estimated 33% (36%) local dissipation for M_2 in the LS with (without) the remote effect of the Mariana Island Arc. The differences in these model-estimated energy budgets may be due to a variety of different model configurations, such as the vertical and horizontal resolutions, bathymetry, background stratification, and currents, and parameterizations representing the unresolved physical processes (Di Lorenzo et al. 2006). At this time it is difficult to verify these estimates because of the spatial sparsity of observations.

The energy budget in the SCS is quite different than that in the LS (Fig. 5). The Conv in the SCS is 5.0–7.5 GW, which is roughly $\frac{1}{6}$ to $\frac{1}{4}$ of that in the LS. The DivF in the SCS is negative, indicating that the SCS is a convergence region of baroclinic energy. The magnitude of DivF in the SCS is almost equal to the baroclinic energy propagating from the LS (F_{west}), revealing that the internal tides radiated from the LS are an important energy source for the baroclinic energy dissipation in the SCS. Furthermore, the magnitude of DivF is nearly 2
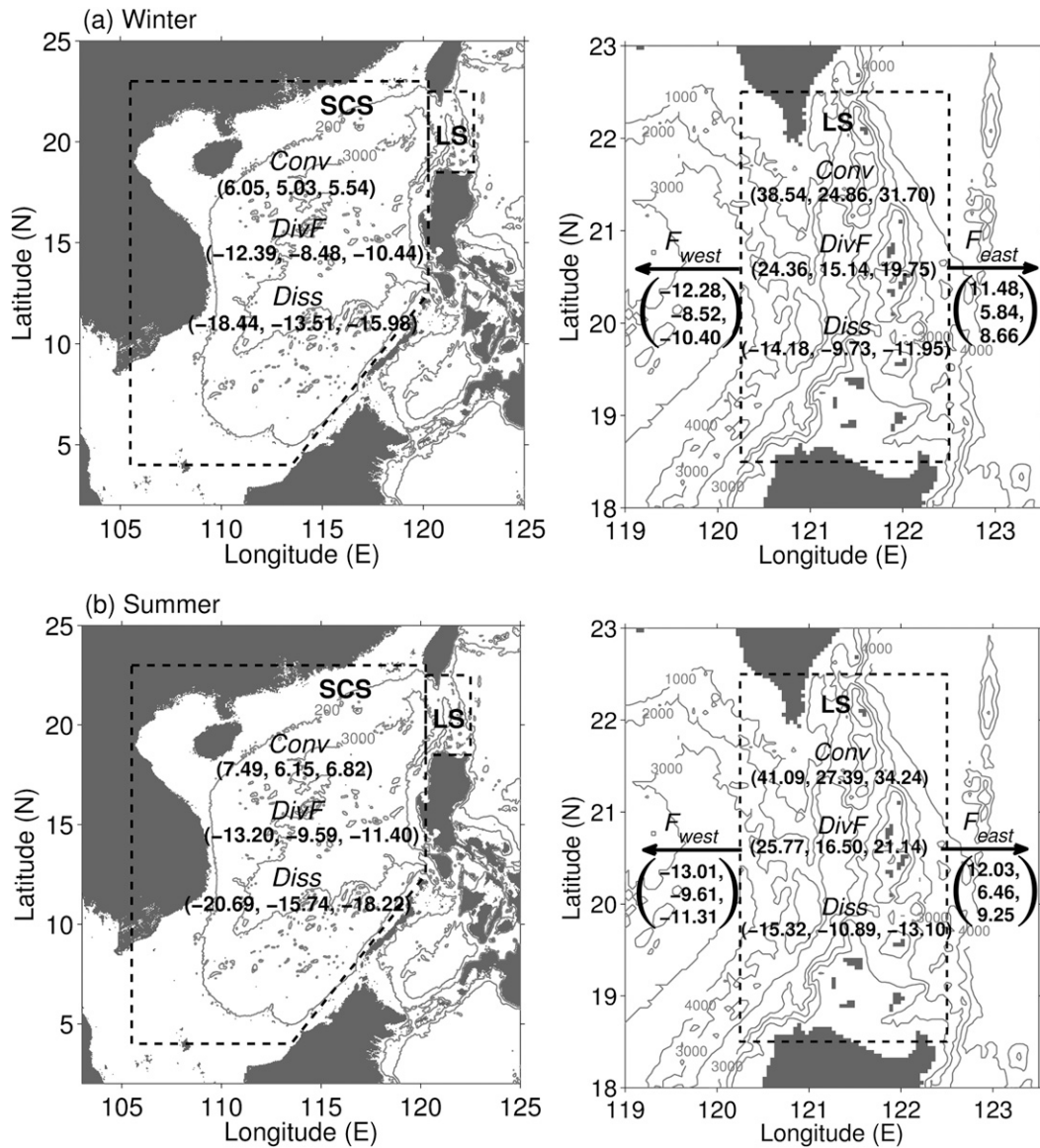
FIG. 5. Diagrams of the internal tides energy budget of the SCS and LS in (a) winter and (b) summer. The two black dashed boxes bound the integral areas of the SCS and LS, respectively. The Conv, DivF, and Diss denote the area-integrated conversion rate from barotropic to baroclinic tidal energy, divergence of baroclinic energy flux, and dissipation rate of the baroclinic energy (GW), respectively. The F_{west} and F_{east} denote the meridional section-integrated baroclinic energy (GW) on the west and east boundaries of dashed box, respectively. The three numbers in brackets are the values of each physical quantity (Conv, DivF, Diss, F_{west}, or F_{east}) for the spring tide, neap tide, and seasonal mean. The gray contours represent the isobaths.

times Conv in the SCS, suggesting that it is the remotely generated internal tides that play a more dominant role in sustaining the baroclinic tidal dissipation in the SCS.

The depth-integrated baroclinic energy flux vectors in the LS and northern SCS during the spring tide in summer are shown in Fig. 6a. One can see that the two ridges in the LS are the main sites of internal-tide generation. At the northern part of the LS, the eastern ridge generates appreciable eastward signals. Energy fluxes

westward into the northern SCS with the maximum exceeding $60 \, kW \, m^{-1}$ occur at the southern part of the western ridge. It appears that flux vectors swirl clockwise, with northward (southward) fluxes over the western (eastern) ridges. The above patterns, together with the high energy flux values, are consistent with the measurement and model report by Alford et al. (2011). The primary beam of internal wave energy generated in the LS points directly toward the Dongsha Plateau. The
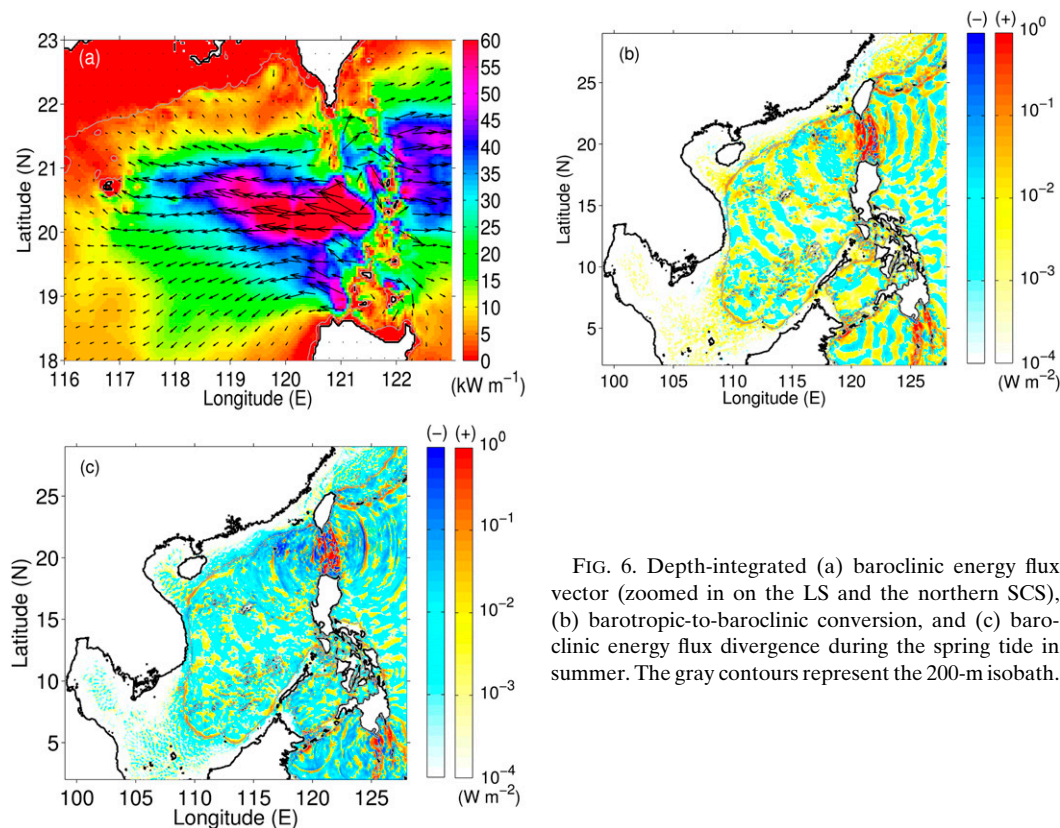
FIG. 6. Depth-integrated (a) baroclinic energy flux vector (zoomed in on the LS and the northern SCS), (b) barotropic-to-baroclinic conversion, and (c) baroclinic energy flux divergence during the spring tide in summer. The gray contours represent the 200-m isobath.

energy flux is about 5–15 kW m^{-1} on the continental slope and less than 5 kW m^{-1} on the continental shelf, comparable to the values reported by previous studies (St. Laurent 2008; Klymak et al. 2011).

The spatial distributions of the depth-integrated barotropic-to-baroclinic conversion (Fig. 6b) and the divergence of depth-integrated baroclinic energy flux (Fig. 6c) are all heterogeneous with spatial variations of several orders of magnitude in intensity. Because patterns obtained from different runs are similar, only the results during the spring tide in summer are shown here. Positive energy conversion implies the generation of internal tides, and it shows that a large amount of internal tides are generated along the two ridges of LS. Negative conversion represents the energy transfer from the baroclinic tide to the barotropic tide, which occurs when the phase differences between the density perturbation and the barotropic vertical velocity are greater than 90° (Zilberman et al. 2009). This is due to the alteration of the phase of density perturbation by remotely generated internal tides, and thus negative conversion indicates multiple generation sites (Carter et al. 2012). Specifically, the negative conversion in the LS is due to the interaction between the internal tides generated at the two adjacent ridges, while that within

the SCS is caused by the interaction between the internal tides radiated from the LS (Fig. 6a) and those generated locally. Figure 6c illustrates the divergence of depth-integrated baroclinic energy flux. Most positive divergence occurs within the LS; however, the negative value dominates in the SCS, indicating that the LS is a source region of internal-tide energy while the SCS is a sink region. On the whole, the baroclinic energy budget analysis reveals that remotely generated internal tides (e.g., those radiated from the LS) impose a great impact on the baroclinic tidal dissipation in the SCS mainly in two ways concurrently: one is to provide enormous baroclinic tidal energy, and the other is to modify the local barotropic-to-baroclinic energy conversion.

c. Dissipation and mixing

In this subsection, we present our estimate of the baroclinic tidal energy dissipation and diapycnal mixing in several selected subregions. Since the seasonal variations are not the focus of this study, the three-dimensional distributions of dissipation rate and diapycnal diffusivity shown below are based on the annual-mean depth-integrated dissipation by taking the average of two seasons' results.
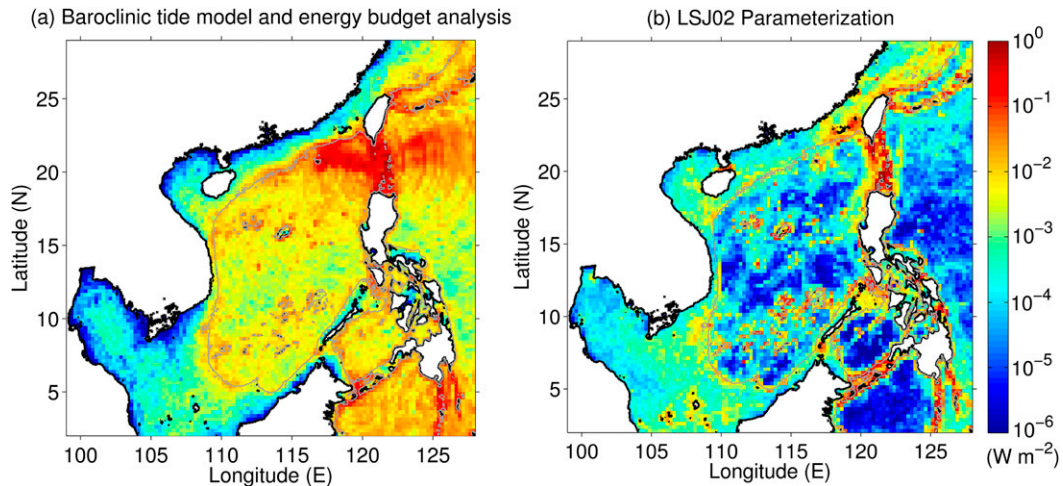
FIG. 7. Annual-mean depth-integrated dissipation rate of baroclinic energy estimated by (a) the baroclinic tide model and energy budget analysis as well as (b) the LSJ02 parameterization. The gray contours represent the 200-m isobath.

Taking the average over each $0.25° \times 0.25°$ grid area, we obtain the climatologically annual-mean depth-integrated dissipation rate of internal tides in the entire LS and SCS region, as shown in Fig. 7a. The strong dissipation in the SCS occurs mainly in the northern region to the west of LS within water deeper than the 200-m isobath. The dissipation rate in the central and southern SCS is about one or two orders of magnitude weaker, except near some rough topography like the shelf breaks, islands, and abrupt seamounts. Moreover, the dissipation rate in the coastal area shallower than 200-m isobath is much weaker than that in the deep basin of SCS, implying that much of the baroclinic energy of internal tides dissipates and/or reflects before reaching the continental shelf off China. As shown in Fig. 7b, except for some high patches atop the LS ridges, the dissipation rate from the LSJ02 parameterization is generally one to two orders of magnitude weaker than that from the baroclinic tide model and energy budget analysis (Fig. 7a), especially in the abyssal basin of SCS. This difference is because the LSJ02 parameterization is based on the assumption that dissipation is associated with locally generated internal tides, without taking into account the contribution of energy dissipation due to remotely generated internal tides.

The depth-integrated energy dissipation maps, as well as the cross-section distributions of dissipation rate and diapycnal diffusivity in several selected subregions, are presented in Figs. 8–10. In the LS region (Fig. 8), our results clearly show that extremely enhanced mixing dominates this area. The elevated depth-integrated energy dissipation reaches $O(1)\,\mathrm{W\,m^{-2}}$ atop two subsurface ridges and is one order of magnitude weaker

near the flanks (Fig. 8a). High values of dissipation rate exceeding $O(10^{-7})\,\mathrm{W\,kg^{-1}}$ accompanied by the diapycnal diffusivity about $O(10^{-2})\,\mathrm{m^2\,s^{-1}}$ occur in the deep water (Figs. 8b,c). A background diapycnal diffusivity of only $O(10^{-5})\,\mathrm{m^2\,s^{-1}}$ appears in the upper 1000-m water column of the Luzon Trough, whereas values greater than $O(10^{-3})\,\mathrm{m^2\,s^{-1}}$ are found below 1500-m depth, with the peak values of $O(10^{-1})\,\mathrm{m^2\,s^{-1}}$ occurring in some patches near the bottom (Fig. 8c). The above dissipation and mixing patterns as well as their magnitudes in the LS region are comparable to the upper bound value of the observational report by Tian et al. (2009) based on the finescale shear–strain parameterization and the results given by Alford et al. (2011) using the Thorpe-scale method.

Waves generated from multiple nearby sources interfere with each other, which can complicate the patterns of wave kinematics and energy fluxes (Rainville et al. 2010; Zhao et al. 2010) and affect wave scattering and transmission (Klymak et al. 2011). Interference between incident baroclinic waves and local barotropic forcing can greatly alter the property and magnitude of local barotropic to baroclinic conversion (Kelly and Nash 2010). Alford et al. (2011) speculated that at least part of internal-tide dissipation in the LS is owed to the resonance between the two ridges, and we postulate that this process can take effect during the simulation of internal tides. Alford et al. (2011) considered that the northern ridge spacing is favorable for the interaction between semidiurnal signals generated at the two ridges and hence the enhanced conversion there, leading to the stronger dissipation observed at the northern part than along the southern part, which also exhibits in our results.
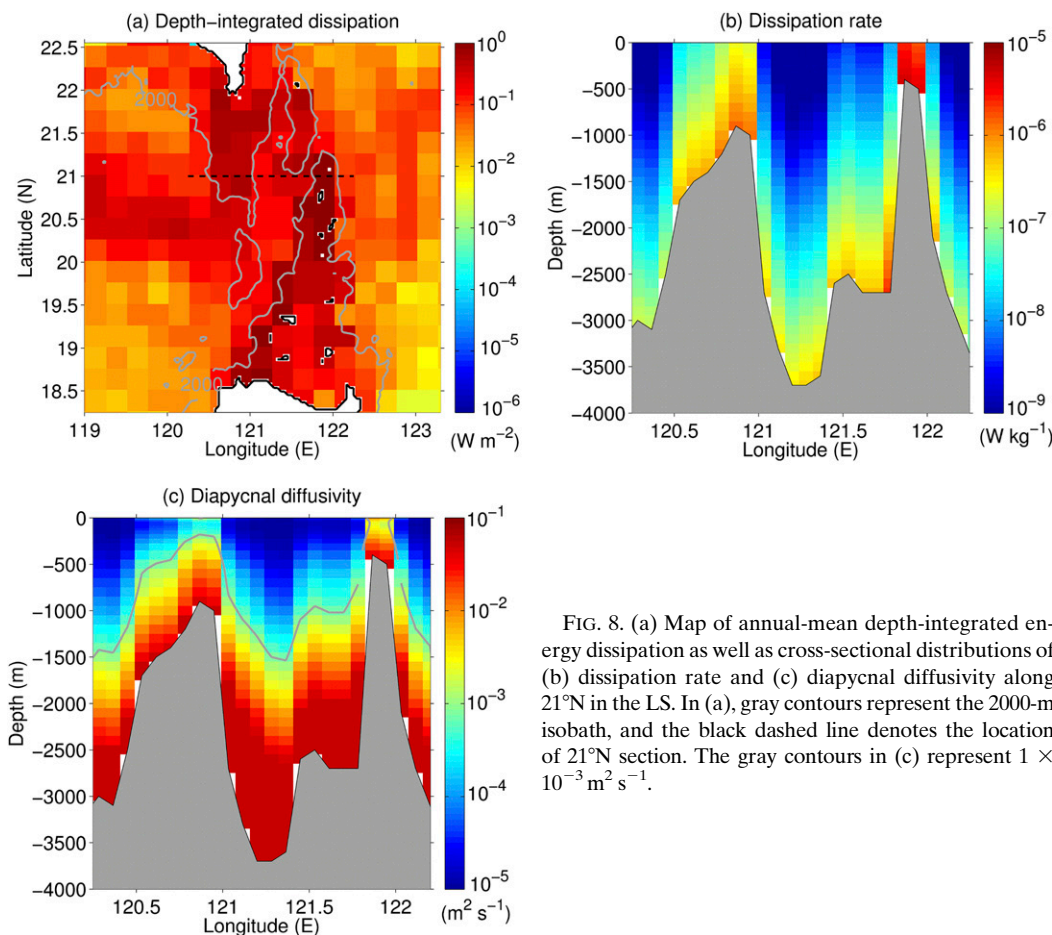
FIG. 8. (a) Map of annual-mean depth-integrated energy dissipation as well as cross-sectional distributions of (b) dissipation rate and (c) diapycnal diffusivity along 21°N in the LS. In (a), gray contours represent the 2000-m isobath, and the black dashed line denotes the location of 21°N section. The gray contours in (c) represent $1 \times 10^{-3}\,\mathrm{m}^2\,\mathrm{s}^{-1}$.

In the continental margin of the northern SCS (Fig. 9), strong tidal dissipation can appear in the upper layer of shallow water, and the most intense turbulent dissipation occurs in the shelfbreak region, with depth-integrated energy dissipation, dissipation rate, and diapycnal diffusivity reaching $O(10^{-2}$–$10^{-1})\,\mathrm{W}\,\mathrm{m}^{-2}$, $O(10^{-7}$–$10^{-6})\,\mathrm{W}\,\mathrm{kg}^{-1}$, and $O(10^{-4}$–$10^{-3})\,\mathrm{m}^2\,\mathrm{s}^{-1}$ respectively, which are one to two orders of magnitude larger than the typical levels in open oceans (Munk and Wunsch 1998). While over the shelf and slope regions, the dissipation is weaker than that in the shelfbreak region. In particular, more energy is lost in the east of the Dongsha Plateau (Fig. 9a), where the bottom topography abruptly shoals from 3000 to 500 m and shallower, with the intense depth-integrated energy dissipation up to $O(1)\,\mathrm{W}\,\mathrm{m}^{-2}$, which is comparable to that in the LS (Fig. 8a). The above pattern and values in the continental margin of the northern SCS are in agreement with the previous findings through time series microstructure measurements (St. Laurent 2008; St. Laurent et al. 2011; Yang et al. 2014) and mooring data (Klymak et al. 2011).

The previous reports about the nonlinear waves on the continental slope, shelf break, and shelf of the northern SCS generally suggest that the turbulent mixing in these regions is mainly related to the transformation of nonlinear internal solitonlike waves during the wave-shoaling process (e.g., Orr and Mignerey 2003). However, Klymak et al. (2011) pointed out that there is little chance for the solitons at higher frequencies to interact with the seafloor, and the strong dissipation observed near the seafloor on the continental shelf break is associated with the near-bottom baroclinic currents rather than the solitary waves. Our baroclinic tide model has a spatial resolution of ~5 km and therefore cannot produce nonlinear internal waves that have a horizontal scale of 1–2 km. Hence, the enhanced dissipation estimated here may attribute to the interaction of both locally and remotely generated internal tides with the continental topography, which supports the view of Klymak et al. (2011).

Along the 21°N section of the northern SCS (Figs. 10a,b), it reveals that elevated levels of turbulence, with a dissipation rate reaching $O(10^{-7})\,\mathrm{W}\,\mathrm{kg}^{-1}$ and diapycnal
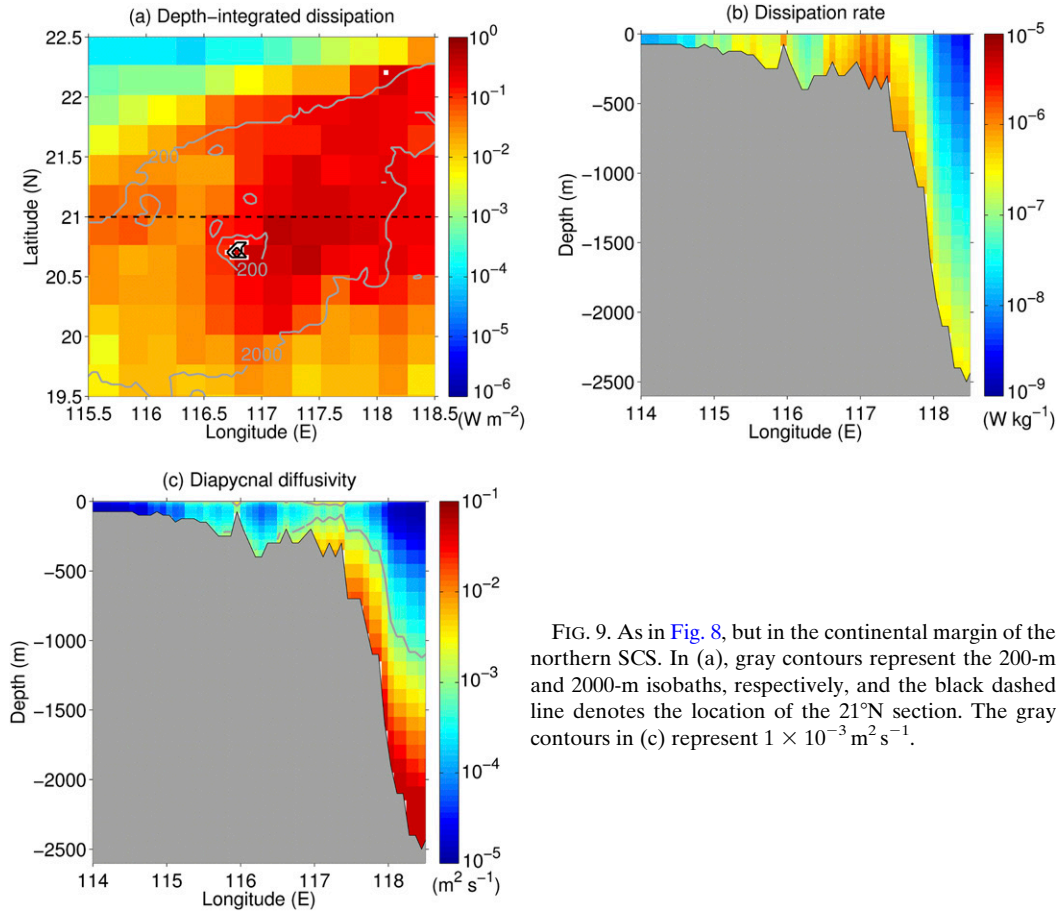
FIG. 9. As in Fig. 8, but in the continental margin of the northern SCS. In (a), gray contours represent the 200-m and 2000-m isobaths, respectively, and the black dashed line denotes the location of the 21°N section. The gray contours in (c) represent $1 \times 10^{-3}\,\mathrm{m}^2\,\mathrm{s}^{-1}$.

diffusivity up to $O(10^{-3}–10^{-1})\,\mathrm{m}^2\,\mathrm{s}^{-1}$, exist in the deep northern SCS within ~2000-m water column above the seafloor, which are consistent with the only report so far along the same section by Tian et al. (2009) based on in situ observations and finescale shear–strain parameterization. While along the 115°N section across the Zhongsha and Nansha reefs in the central and southern deep-water basin of SCS (Figs. 10c,d), dissipation and mixing levels are elevated in the bottom 500–1000 m over rough topography such as seamounts and reefs, with dissipation rate and diapycnal diffusivity on the order of $O(10^{-8})\,\mathrm{W\,kg}^{-1}$ and $O(10^{-3})\,\mathrm{m}^2\,\mathrm{s}^{-1}$, respectively.

The estimate of Klymak et al. (2011) based on mooring data indicated that about 33% of the incoming diurnal tidal energy from the LS is reflected back into the SCS deep basin due to the supercritical feature of the continental slope with respect to the diurnal tide. As a result, the mixing in the deep water of the SCS can be enhanced by the superposition of incident and reflected wave packets (Althaus et al. 2003). Moreover, the interaction between the remotely generated internal waves (e.g., those radiated from the LS) and the rough bottom topography of the SCS can partially induce the intense mixing in the deep water.

5. Summary and discussion

In this paper, the tidal dissipation and mixing in the LS and SCS are investigated through internal-tide simulation and baroclinic energy budget analysis, considering both the locally and remotely generated internal tides. Baroclinic energy budget analysis reveals that the internal tides radiated from the LS are the dominant energy source for the tidal dissipations in the SCS. Moreover, a preliminary three-dimensional climatological-mean diapycnal diffusivity field is obtained, which is characterized by the intense turbulent mixing driven by energy dissipation of both locally and remotely generated internal tides in the LS and SCS. Our results are comparable with previous observations based on microstructure measurements or estimates by finescale parameterizations but are one to two orders of magnitudes larger than those by the LSJ02 parameterization (which takes into account the effect of local tidal
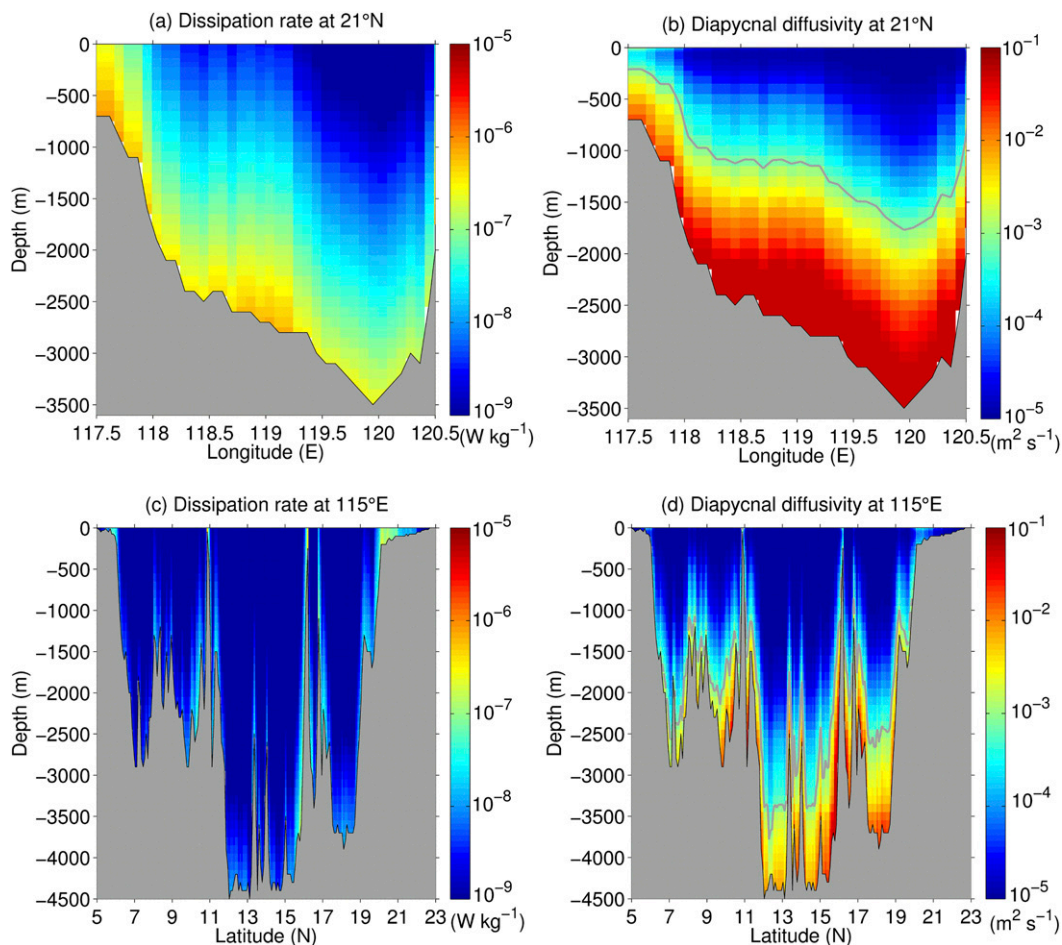
FIG. 10. Cross-sectional distributions of (a),(c) dissipation rate and (b),(d) diapycnal diffusivity along (top) 21°N and (bottom) 115°E in the deep basin of SCS. The gray contours in (b) and (d) represent $1 \times 10^{-3}\,\mathrm{m^2\,s^{-1}}$.

dissipation only). Therefore, the effect of remotely generated internal tides is very important and should be taken into account in the tidal mixing estimate of the marginal seas like the SCS, where a large part of internal tides is not locally generated but is generated from the adjacent prominent bathymetry like the LS.

To the best of our knowledge, there are no direct measurements of dissipation made in the deep-water basin of the northern SCS between the LS and the continental margin and in the central and southern regions of the SCS deep basin; in fact, turbulent dissipation over these regions remains largely unknown. Therefore, more observations in the SCS deep basin are urgently needed to validate the intense turbulent dissipation and mixing estimated in this study.

The three-dimensional climatological field of diapycnal diffusivity obtained in our study may provide a more comprehensive and realistic description of the turbulent mixing levels in the LS and SCS by taking into account the effect of both locally and remotely generated internal tides. However, our estimates are based on a regional baroclinic tide model with the horizontally homogeneous stratification and the rather crude energy analysis with the vertically integrated energy constraint. Actually, the temporally and spatially varying stratification, general ocean circulation (e.g., the Kuroshio), and background internal-tide fields (e.g., remotely generated internal tides from the Mariana Arc) could noticeably modulate the processes of internal-tide generation, propagation, and dissipation in the LS (Jan et al. 2012; Kerry et al. 2013, 2014) and hence influence those in the SCS. As such, our estimate may be biased. Further study based on more realistic energy constraint could provide better description of tidal mixing in the SCS.

TABLE A1. Sensitivity experiments of dissipation parameters for the LS domain.

Experiment	A_h (m^2 s^{-1})	A_v (m^2 s^{-1})	C_d	Conversion	Energy flux divergence	Dissipation (energetics based)	Dissipation (directly computed)
				(GW) (relative change to experiments CTRL)			
CTRL	10	1×10^{-4}	2.5×10^{-3}	41.09	25.77	-15.32	-6.84
E1	1	1×10^{-4}	2.5×10^{-3}	41.31 (+0.5%)	25.85 (+0.3%)	-15.46 (+0.9%)	-5.48 (-19.9%)
E2	100	1×10^{-4}	2.5×10^{-3}	40.67 (-1.0%)	25.51 (-1.0%)	-15.16 (-1.0%)	-10.51 (+53.7%)
E3	10	1×10^{-5}	2.5×10^{-3}	40.97 (-2.9%)	25.87 (+0.4%)	-14.80 (-3.4%)	-6.41 (-6.3%)
E4	10	1×10^{-3}	2.5×10^{-3}	40.97 (-2.9%)	25.57 (-0.8%)	-15.40 (+0.5%)	-11.15 (+63.0%)
E5	10	1×10^{-4}	2.5×10^{-4}	41.14 (+1.2%)	25.21 (-2.9%)	-15.93 (+4.0%)	-5.14 (-24.9%)
E6	10	1×10^{-4}	2.5×10^{-2}	42.95 (+4.5%)	26.92 (+4.5%)	-16.03 (+4.6%)	-14.50 (+112.0%)

APPENDIX

Sensitivity of Internal-Tide Simulation to Dissipation Parameters

The baroclinic dissipation can be estimated from the tidal period–averaged energy balance relation:

$$-\langle E_{bt2bc} \rangle + \langle \nabla_h \cdot \mathbf{F}_{bc} \rangle$$
$$\approx \langle DIS_{bc} \rangle$$
$$= \langle DIS_{dir} \rangle + \text{numerical dissipation} + \text{errors}, \quad (A1)$$

where $\langle \cdot \rangle$ represents the tidal period mean. The term $\langle DIS_{bc} \rangle$ is the energetics-based baroclinic dissipation as the residual of the baroclinic energy budget, while $\langle DIS_{dir} \rangle$ is the directly computed dissipation given as

$$\langle DIS_{dir} \rangle = -\left\langle \int_{-H}^{\eta} \varepsilon_{visc} \, dz + \varepsilon_{bd} \right\rangle, \quad (A2)$$

$$\varepsilon_{visc} = \rho_0 A_h \nabla_h \mathbf{u}' \cdot \nabla_h \mathbf{u}' + \rho_0 A_v \frac{\partial \mathbf{u}'}{\partial z} \cdot \frac{\partial \mathbf{u}'}{\partial z}, \quad (A3)$$

and

$$\varepsilon_{bd} = \rho_0 C_d |\mathbf{u}|(uu' + vv') \quad \text{at} \quad z = -H, \quad (A4)$$

where ε_{visc} and ε_{bd} are the energy dissipation rates caused by viscosity and bottom drag, respectively, ρ_0 is the constant reference density, C_d is the bottom drag coefficient, and $\mathbf{u} = (u, v)$ is the horizontal velocity (Kang and Fringer 2012; Nagai and Hibiya 2015). Errors arise from the assumption that the tendency term should tend to zero for a periodic system as well as from other neglected terms of the energy budget. Numerical dissipation primarily results from the numerical diffusion related to momentum and scalar advection.

To examine the sensitivity of the simulated internal-tide energy to the viscosity A_h and A_v and bottom drag coefficient C_d, a set of numerical experiments for summer are carried out. The reference experiment CTRL employs $A_h = 10 \text{ m}^2 \text{ s}^{-1}$, $A_v = 1 \times 10^{-4} \text{ m}^2 \text{ s}^{-1}$, and $C_d = 2.5 \times 10^{-3}$. In sensitivity experiments (E1–E6), one variable from the group of three (A_h, A_v, or C_d) is increased or reduced by one order of magnitude with respect to that of CTRL. For each experiment, we calculated the barotropic-to-baroclinic conversion [Eq. (6)], the baroclinic energy flux divergence

TABLE A2. Sensitivity experiments of dissipation parameters for the SCS domain.

Experiment	A_h (m^2 s^{-1})	A_v (m^2 s^{-1})	C_d	Conversion	Energy flux divergence	Dissipation (energetics based)	Dissipation (directly computed)
				(GW) (relative change to experiments CTRL)			
CTRL	10	1×10^{-4}	2.5×10^{-3}	7.49	-13.20	-20.69	-8.04
E1	1	1×10^{-4}	2.5×10^{-3}	7.45 (-0.5%)	-13.06 (-1.1%)	-20.51 (-0.9%)	-7.74 (-3.7%)
E2	100	1×10^{-4}	2.5×10^{-3}	7.37 (-1.6%)	-12.90 (-2.3%)	-20.27 (-2.0%)	-10.44 (+29.9%)
E3	10	1×10^{-5}	2.5×10^{-3}	7.50 (+1.0%)	-13.30 (+0.7%)	-20.80 (+0.5%)	-7.09 (-11.8%)
E4	10	1×10^{-3}	2.5×10^{-3}	7.41 (-1.1%)	-13.15 (-0.4%)	-20.56 (-0.6%)	-14.52 (+80.6%)
E5	10	1×10^{-4}	2.5×10^{-4}	7.80 (+4.1%)	-12.76 (-3.3%)	-20.56 (-0.6%)	-7.66 (-4.7%)
E6	10	1×10^{-4}	2.5×10^{-2}	7.20 (-3.8%)	-13.91 (+5.4%)	-21.11 (+2.0%)	-15.17 (+88.7%)

[Eq. (7)], the energetics-based baroclinic dissipation [Eq. (5)], and the directly computed baroclinic dissipation [Eq. (A2)] averaged over a 2-day period during the spring tide and integrated within the LS and the SCS domains. The results are summarized in Tables A1 and A2.

Compared with experiment CTRL, changing the dissipation parameters by one order of magnitude has a minor impact on the conversion, divergence, and hence the energetics-based dissipation, with the relative changes less than 6% for both the LS and the SCS domains. However, the directly computed dissipation changes appreciably with the employed values of dissipation parameters. Increasing (reducing) A_h, A_v, or C_d by one order of magnitude causes 54%–112% increase (6%–25% decrease) in the directly computed dissipation for the LS domain and 30%–89% increase (4%–12% decrease) in that for the SCS domain. Overall, this set of sensitivity experiments suggest that the barotropic-to-baroclinic conversion, the baroclinic energy flux divergence, and the energetics-based dissipation are not significantly sensitive to the dissipation parameters, whereas the directly computed dissipation depends greatly on the dissipation parameters. Based on the balance relation equation [Eq. (A1)], the numerical dissipation and errors are thus also strong functions of the dissipation parameters.

In the ocean models, the values of dissipation parameters are chosen for the stability requirements of simulations instead of the real ocean values. Besides, the viscosities and bottom drag coefficient in the realistic ocean vary with location and time, but a constant value for each throughout the domain is set in these experiments. Therefore, the directly computed dissipation may not represent the true physical dissipation in the realistic ocean (Kang and Fringer 2012).

For these reasons, in this paper, the simplified baroclinic energy budget balance equation [Eq. (5)] is used for the baroclinic energy analysis. Note that this energetics-based baroclinic energy dissipation $\langle \text{DIS}_{bc} \rangle$ includes both the physical dissipation and the biases due to the numerical dissipation and computation errors and thus may be somewhat overestimated.

REFERENCES

Alford, M. H., and Coauthors, 2011: Energy flux and dissipation in Luzon Strait: Two tales of two ridges. *J. Phys. Oceanogr.*, **41**, 2211–2222, doi:10.1175/JPO-D-11-073.1.

——, and Coauthors, 2015: The formation and fate of internal waves in the South China Sea. *Nature*, **521**, 65–69, doi:10.1038/nature14399.

Althaus, A. M., E. Kunze, and T. B. Sanford, 2003: Internal tide radiation from Mendocino Escarpment. *J. Phys. Oceanogr.*, **33**, 1510–1527, doi:10.1175/1520-0485(2003)033<1510:ITRFME>2.0.CO;2.

Bell, T. H., 1975: Topographically generated internal waves in the open ocean. *J. Geophys. Res.*, **80**, 320–327, doi:10.1029/JC080i003p00320.

Bryan, K., and L. J. Lewis, 1979: A water mass model of the World Ocean. *J. Geophys. Res.*, **84**, 2503–2517, doi:10.1029/JC084iC05p02503.

Buijsman, M. C., S. Legg, and J. M. Klymak, 2012: Double-ridge internal tide interference and its effect on dissipation in Luzon Strait. *J. Phys. Oceanogr.*, **42**, 1337–1356, doi:10.1175/JPO-D-11-0210.1.

——, and Coauthors, 2014: Three-dimensional double-ridge internal tide resonance in Luzon Strait. *J. Phys. Oceanogr.*, **44**, 850–869, doi:10.1175/JPO-D-13-024.1.

Carter, G. S., and M. C. Gregg, 2002: Intense variable mixing near the head of Monterey Submarine Canyon. *J. Phys. Oceanogr.*, **32**, 3145–3165, doi:10.1175/1520-0485(2002)032<3145:IVMNTH>2.0.CO;2.

——, O. B. Fringer, and E. D. Zaron, 2012: Regional models of internal tides. *Oceanography*, **25**, 56–65, doi:10.5670/oceanog.2012.42.

Chang, Y. T., W. L. Hsu, J. H. Tai, T. Y. Tang, M. H. Chang, and S. Y. Chao, 2010: Cold deep water in the South China Sea. *J. Oceanogr.*, **66**, 183–190, doi:10.1007/s10872-010-0016-x.

Chao, S. Y., D. S. Ko, R. C. Lien, and P. T. Shaw, 2007: Assessing the west ridge of Luzon Strait as an internal wave mediator. *J. Oceanogr.*, **63**, 897–911, doi:10.1007/s10872-007-0076-8.

Di Lorenzo, E., W. R. Young, and S. L. Smith, 2006: Numerical and analytical estimates of M_2 tidal conversion at steep oceanic ridges. *J. Phys. Oceanogr.*, **36**, 1072–1084, doi:10.1175/JPO2880.1.

Duda, T. F., and L. Rainville, 2008: Diurnal and semidiurnal internal tide energy flux at a continental slope in the South China Sea. *J. Geophys. Res.*, **113**, C03025, doi:10.1029/2007JC004418.

Egbert, G. D., and R. D. Ray, 2000: Significant dissipation of tidal energy in the deep ocean inferred from satellite altimeter data. *Nature*, **405**, 775–778, doi:10.1038/35015531.

——, and S. Y. Erofeeva, 2002: Efficient inverse modeling of barotropic ocean tides. *J. Atmos. Oceanic Technol.*, **19**, 183–204, doi:10.1175/1520-0426(2002)019<0183:EIMOBO>2.0.CO;2.

——, A. F. Bennett, and M. G. G. Foreman, 1994: TOPEX/POSEIDON tides estimated using a global inverse model. *J. Geophys. Res.*, **99**, 24 821–24 852, doi:10.1029/94JC01894.

Ferron, B., H. Mercier, K. Speer, A. Gargett, and K. Polzin, 1998: Mixing in the Romanche Fracture Zone. *J. Phys. Oceanogr.*, **28**, 1929–1945, doi:10.1175/1520-0485(1998)028<1929:MITRFZ>2.0.CO;2.

Friedrich, T., A. Timmermann, T. Decloedt, D. S. Luther, and A. Mouchet, 2011: The effect of topography-enhanced diapycnal mixing on ocean and atmospheric circulation and marine biogeochemistry. *Ocean Modell.*, **39**, 262–274, doi:10.1016/j.ocemod.2011.04.012.

Guo, P., W. Fang, C. Liu, and F. Qiu, 2012: Seasonal characteristics of internal tides on the continental shelf in the northern South China Sea. *J. Geophys. Res.*, **117**, C04023, doi:10.1029/2011JC007215.

Huang, R. X., 1999: Mixing and energetics of the oceanic thermohaline circulation. *J. Phys. Oceanogr.*, **29**, 727–746, doi:10.1175/1520-0485(1999)029<0727:MAEOTO>2.0.CO;2.

Jan, S., C. S. Chern, J. Wang, and S. Y. Chao, 2007: Generation of diurnal K_1 internal tide in the Luzon Strait and its influence on surface tide in the South China Sea. *J. Geophys. Res.*, **112**, C06019, doi:10.1029/2006JC004003.

——, R. C. Lien, and C. H. Ting, 2008: Numerical study of baroclinic tides in Luzon Strait. *J. Oceanogr.*, **64**, 789–802, doi:10.1007/s10872-008-0066-5.

——, C. S. Chern, J. Wang, and M. D. Chiou, 2012: Generation and propagation of baroclinic tides modified by the Kuroshio in the Luzon Strait. *J. Geophys. Res.*, **117**, C02019, doi:10.1029/2011JC007229.

Jayne, S. R., 2009: The impact of abyssal mixing parameterizations in an ocean general circulation model. *J. Phys. Oceanogr.*, **39**, 1756–1775, doi:10.1175/2009JPO4085.1.

——, and L. C. St. Laurent, 2001: Parameterizing tidal dissipation over rough topography. *Geophys. Res. Lett.*, **28**, 811–814, doi:10.1029/2000GL012044.

Kang, D., and O. Fringer, 2012: Energetics of barotropic and baroclinic tides in the Monterey Bay area. *J. Phys. Oceanogr.*, **42**, 272–290, doi:10.1175/JPO-D-11-039.1.

Kelly, S. M., and J. D. Nash, 2010: Internal-tide generation and destruction by shoaling internal tides. *Geophys. Res. Lett.*, **37**, L23611, doi:10.1029/2010GL045598.

Kerry, C. G., B. S. Powell, and G. S. Carter, 2013: Effects of remote generation sites on model estimates of M_2 internal tides in the Philippine Sea. *J. Phys. Oceanogr.*, **43**, 187–204, doi:10.1175/JPO-D-12-081.1.

——, ——, and ——, 2014: The impact of subtidal circulation on internal tide generation and propagation in the Philippine Sea. *J. Phys. Oceanogr.*, **44**, 1386–1405, doi:10.1175/JPO-D-13-0142.1.

Klymak, J. M., M. H. Alford, R. Pinkel, R.-C. Lien, Y. J. Yang, and T.-Y. Tang, 2011: The breaking and scattering of the internal tide on a continental slope. *J. Phys. Oceanogr.*, **41**, 926–945, doi:10.1175/2010JPO4500.1.

Kunze, E., and J. M. Toole, 1997: Tidally driven vorticity, diurnal shear, and turbulence atop Fieberling Seamount. *J. Phys. Oceanogr.*, **27**, 2663–2693, doi:10.1175/1520-0485(1997)027<2663:TDVDSA>2.0.CO;2.

Large, W. G., J. C. McWilliams, and S. C. Doney, 1994: Oceanic vertical mixing: A review and a model with a nonlocal boundary layer parameterization. *Rev. Geophys.*, **32**, 363–403, doi:10.1029/94RG01872.

Ledwell, J. R., A. J. Watson, and C. S. Law, 1993: Evidence for slow mixing across the pycnocline from an open-ocean tracer release experiment. *Nature*, **364**, 701–703, doi:10.1038/364701a0.

——, E. T. Montgomery, K. L. Polzin, L. C. St. Laurent, R. W. Schmitt, and J. M. Toole, 2000: Evidence of enhanced mixing over rough topography in the abyssal ocean. *Nature*, **403**, 179–182, doi:10.1038/35003164.

Lozovatsky, I., Z. Liu, H. J. S. Fernando, J. Hu, and H. Wei, 2013: The TKE dissipation rate in the northern South China Sea. *Ocean Dyn.*, **63**, 1189–1201, doi:10.1007/s10236-013-0656-7.

Ma, B. B., R. C. Lien, and D. S. Ko, 2013: The variability of internal tides in the northern South China Sea. *J. Oceanogr.*, **69**, 619–630, doi:10.1007/s10872-013-0198-0.

MacKinnon, J., 2013: Mountain waves in the deep ocean. *Nature*, **501**, 321–322, doi:10.1038/501321a.

——, and M. C. Gregg, 2003: Mixing on the late-summer New England shelf—Solibores, shear, and stratification. *J. Phys. Oceanogr.*, **33**, 1476–1492, doi:10.1175/1520-0485(2003)033<1476:MOTLNE>2.0.CO;2.

Marshall, J., and K. G. Speer, 2012: Closure of the meridional overturning circulation through Southern Ocean upwelling. *Nat. Geosci.*, **5**, 171–180, doi:10.1038/ngeo1391.

——, A. Adcroft, C. Hill, L. Perelman, and C. Heisey, 1997: A finite-volume, incompressible Navier Stokes model for studies of the ocean on parallel computers. *J. Geophys. Res.*, **102**, 5753–5766, doi:10.1029/96JC02775.

Melet, A., R. W. Hallberg, S. Legg, and K. Polzin, 2013: Sensitivity of the ocean state to the vertical distribution of internal-tide-driven mixing. *J. Phys. Oceanogr.*, **43**, 602–615, doi:10.1175/JPO-D-12-055.1.

Mellor, G. L., 2004: Users guide for a three-dimensional, primitive equation, numerical ocean model. Princeton University Rep., 56 pp.

——, and T. Yamada, 1982: Development of a turbulence closure model for geophysical fluid problems. *Rev. Geophys.*, **20**, 851–875, doi:10.1029/RG020i004p00851.

Munk, W., and C. Wunsch, 1998: Abyssal recipes II: Energetics of tidal and wind mixing. *Deep-Sea Res.*, **45**, 1977–2010, doi:10.1016/S0967-0637(98)00070-3.

Nagai, T., and T. Hibiya, 2015: Internal tides and associated vertical mixing in the Indonesian Archipelago. *J. Geophys. Res. Oceans*, **120**, 3373–3390, doi:10.1002/2014JC010592.

Nash, J. D., M. H. Alford, and E. Kunze, 2005: Estimating internal wave energy fluxes in the ocean. *J. Atmos. Oceanic Technol.*, **22**, 1551–1570, doi:10.1175/JTECH1784.1.

Nikurashin, M., and R. Ferrari, 2013: Overturning circulation driven by breaking internal waves in the deep ocean. *Geophys. Res. Lett.*, **40**, 3133–3137, doi:10.1002/grl.50542.

Niwa, Y., and T. Hibiya, 2004: Three-dimensional numerical simulation of M_2 internal tides in the East China Sea. *J. Geophys. Res.*, **109**, C04027, doi:10.1029/2003JC001923.

——, and ——, 2014: Generation of baroclinic tide energy in a global three-dimensional numerical model with different spatial grid resolutions. *Ocean Modell.*, **80**, 59–73, doi:10.1016/j.ocemod.2014.05.003.

Orr, M. H., and P. C. Mignerey, 2003: Nonlinear internal waves in the South China Sea: Observation of the conversion of depression internal waves to elevation internal waves. *J. Geophys. Res.*, **108**, 3064, doi:10.1029/2001JC001163.

Osborn, T. R., 1980: Estimates of the local rate of vertical diffusion from dissipation measurements. *J. Phys. Oceanogr.*, **10**, 83–89, doi:10.1175/1520-0485(1980)010<0083:EOTLRO>2.0.CO;2.

Pacanowski, R. C., and S. G. H. Philander, 1981: Parameterization of vertical mixing in numerical models of tropical oceans. *J. Phys. Oceanogr.*, **11**, 1443–1451, doi:10.1175/1520-0485(1981)011<1443:POVMIN>2.0.CO;2.

Polzin, K. L., 2004: Idealized solutions for the energy balance of the finescale internal wave field. *J. Phys. Oceanogr.*, **34**, 231–246, doi:10.1175/1520-0485(2004)034<0231:ISFTEB>2.0.CO;2.

——, 2009: An abyssal recipe. *Ocean Modell.*, **30**, 298–309, doi:10.1016/j.ocemod.2009.07.006.

——, J. M. Toole, J. R. Ledwell, and R. W. Schmitt, 1997: Spatial variability of turbulent mixing in the abyssal ocean. *Science*, **276**, 93–96, doi:10.1126/science.276.5309.93.

Qu, T., J. B. Girton, and J. A. Whitehead, 2006: Deepwater overflow through Luzon Strait. *J. Geophys. Res.*, **111**, C01002, doi:10.1029/2005JC003139.

Rahmstorf, S., 2003: Thermohaline circulation: The current climate. *Nature*, **421**, 699, doi:10.1038/421699a.

Rainville, L., T. M. S. Johnston, G. S. Carter, M. A. Merrifield, R. Pinkel, P. Worcester, and B. D. Dushaw, 2010: Interference pattern and propagation of the M_2 internal tide south of the Hawaiian Ridge. *J. Phys. Oceanogr.*, **40**, 311–325, doi:10.1175/2009JPO4256.1.

Ray, R. D., and E. D. Zaron, 2011: Non-stationary internal tides observed with satellite altimetry. *Geophys. Res. Lett.*, **38**, L17609, doi:10.1029/2011GL048617.

Saenko, O. A., and W. J. Merryfield, 2005: On the effect of topographically enhanced mixing on the global ocean circulation. *J. Phys. Oceanogr.*, **35**, 826–834, doi:10.1175/JPO2722.1.

Scott, R. B., J. A. Goff, A. C. Naveira Garabato, and A. J. Nurser, 2011: Global rate and spectral characteristics of internal gravity wave generation by geostrophic flow over topography. *J. Geophys. Res.*, **116**, C09029, doi:10.1029/2011JC007005.

Simmons, H. L., S. R. Jayne, L. C. St. Laurent, and A. J. Weaver, 2004: Tidally driven mixing in a numerical model of the ocean general circulation. *Ocean Modell.*, **6**, 245–263, doi:10.1016/S1463-5003(03)00011-8.

St. Laurent, L. C., 2008: Turbulent dissipation on the margins of the South China Sea. *Geophys. Res. Lett.*, **35**, L23615, doi:10.1029/2008GL035520.

——, H. L. Simmons, and S. R. Jayne, 2002: Estimating tidally driven mixing in the deep ocean. *Geophys. Res. Lett.*, **29**, 2106, doi:10.1029/2002GL015633.

——, ——, T. Y. Tang, and Y. H. Wang, 2011: Turbulent properties of internal waves in the South China Sea. *Oceanography*, **24**, 78–87, doi:10.5670/oceanog.2011.96.

Talley, L. D., 2013: Closure of the global overturning circulation through the Indian, Pacific, and Southern Oceans: Schematics and transports. *Oceanography*, **26**, 80–97, doi:10.5670/oceanog.2013.07.

Tian, J., Q. Yang, X. Liang, L. Xie, D. Hu, F. Wang, and T. Qu, 2006: Observation of Luzon Strait transport. *Geophys. Res. Lett.*, **33**, L19607, doi:10.1029/2006GL026272.

——, ——, and W. Zhao, 2009: Enhanced diapycnal mixing in the South China Sea. *J. Phys. Oceanogr.*, **39**, 3191–3203, doi:10.1175/2009JPO3899.1.

Wunsch, C., and R. Ferrari, 2004: Vertical mixing, energy and the general circulation of the oceans. *Annu. Rev. Fluid Mech.*, **36**, 281–314, doi:10.1146/annurev.fluid.36.050802.122121.

Yang, Q., J. Tian, W. Zhao, X. Liang, and L. Zhou, 2014: Observations of turbulence on the shelf and slope of northern South China Sea. *Deep-Sea Res. I*, **87**, 43–52, doi:10.1016/j.dsr.2014.02.006.

Zhao, W., C. Zhou, J. Tian, Q. Yang, B. Wang, L. Xie, and T. Qu, 2014: Deep water circulation in the Luzon Strait. *J. Geophys. Res. Oceans*, **119**, 790–804, doi:10.1002/2013JC009587.

Zhao, Z., 2014: Internal tide radiation from the Luzon Strait. *J. Geophys. Res. Oceans*, **119**, 5434–5448, doi:10.1002/2014JC010014.

——, M. H. Alford, J. A. MacKinnon, and R. Pinkel, 2010: Long-range propagation of the semidiurnal internal tide from the Hawaiian Ridge. *J. Phys. Oceanogr.*, **40**, 713–736, doi:10.1175/2009JPO4207.1.

Zilberman, N. V., J. M. Becker, M. A. Merrifield, and G. S. Carter, 2009: Model estimates of M_2 internal tide generation over mid-Atlantic ridge topography. *J. Phys. Oceanogr.*, **39**, 2635–2651, doi:10.1175/2008JPO4136.1.